Observation of anisotropic Dirac cones in the topological material Ti_2Te_2P

Gyanendra Dhakal,[1] Firoza Kabir,[1] Ashis K. Nandy,[2,3] Alex Aperis,[2] Anup Pradhan Sakhya,[1] Subhadip Pradhan,[3] Klauss Dimitri,[1] Christopher Sims,[1] Sabin Regmi,[1] M. Mofazzel Hosen,[1] Yangyang Liu,[1] Luis Persaud,[1] Dariusz Kaczorowski,[4] Peter M. Oppeneer,[2] and Madhab Neupane[1,*]

[1]*Department of Physics, University of Central Florida, Orlando, Florida 32816, USA*
[2]*Department of Physics and Astronomy, Uppsala University, P.O. Box 516, S-75120 Uppsala, Sweden*
[3]*School of Physical Sciences, National Institute of Science Education and Research, An OCC of Homi Bhabha National Institute, Jatni 752050, India*
[4]*Institute of Low Temperature and Structure Research, Polish Academy of Sciences, Okolna 2, PL-50-420 Wroclaw, Poland*

(Received 14 June 2021; revised 19 August 2022; accepted 23 August 2022; published 15 September 2022)

Anisotropic bulk Dirac (or Weyl) cones in three-dimensional systems have recently gained intense research interest as they are examples of materials with tilted Dirac (or Weyl) cones indicating the violation of Lorentz invariance. In contrast, the studies on anisotropic surface Dirac cones in topological materials which contribute to anisotropic carrier mobility have been limited. By employing angle-resolved photoemission spectroscopy and first-principles calculations, we reveal the anisotropic surface Dirac dispersion in a tetradymite material Ti_2Te_2P on the (001) plane of the Brillouin zone. We observe quasielliptical Fermi pockets at the $\bar{M}$ point of the Brillouin zone forming the anisotropic surface Dirac cones. Our calculations of the $\mathbb{Z}_2$ indices confirm that the system is topologically nontrivial with multiple topological phases in the same material. In addition, the observed nodal-line-like feature formed by bulk bands makes this system topologically rich.

DOI: 10.1103/PhysRevB.106.125124

I. INTRODUCTION

The experimental discovery of a three-dimensional (3D) topological insulator (TI) in tetradymite Bi_2Se_3 brought about an unprecedented surge of research interests in exotic states of matter [1–8]. This discovery motivated investigations of other novel phases such as the Dirac semimetals, Weyl semimetals, nodal-line semimetals, topological crystalline insulators, Kondo insulators, etc. [9–18]. Not only have the discoveries of these novel states provided new classifications of materials, but a series of compounds with similar electronic behaviors have also been identified. Recently, a great deal of interest has been directed at a series of bismuth- and antimony-based tetradymite crystals as they host a topological surface state while simultaneously possessing a wide bulk band gap, as such a single 2D Dirac cone in the Brillouin zone (BZ) is present [6,7,19–27]. Similarly, angle-resolved photoemission spectroscopy (ARPES) studies of the 221-type compounds isostructural to the tetradymite family such as Zr_2Te_2P and Hf_2Te_2P [28–30] reveal the presence of topological surface states along with multiple fermionic states in the BZ. In Zr_2Te_2P, multiple Dirac cones are reported, among which two Dirac cones reside within the pseudogap. Additionally, it contains a surface-state anisotropic Dirac cone at the $\bar{M}$ point [28]. Another compound of this family, Hf_2Te_2P, possesses multiple topological states, hosting strong TI and weak TI states in a single material. Furthermore, it consists of a one-dimensional Dirac-node arc along a high-symmetry direction which makes this family even more fascinating [30]. Interestingly, the band inversion takes place between the *d* and *p* bands in these compounds in contrast to other tetradymite families which host band inversion between *s* and *p* bands or between *p* bands [27–31].

Most of the well-studied TIs and topological semimetals (TSMs) have isotropic Dirac cones which are dubbed as type-I fermions. Bi_2Se_3, Cd_3As_2, and TaAs are prime examples of materials hosting type-I fermions in TI, Dirac, and Weyl semimetallic states, respectively [6,10,13]. However, very recently topological states with tilted Dirac cones have gained significant attention. Subsequently, type-II Weyl semimetals [32] and type-II Dirac semimetals [33–35] have been discovered in three-dimensional systems. These anisotropic Dirac cones are formed by bulk bands. Type-II fermions have tilted Dirac cones as a result of broken Lorentz invariance, and Dirac or Weyl nodes exist at the contact of electron and hole energy pockets [32]. In a similar fashion, anisotropic Dirac cones have been reported in two-dimensional systems in which Fermi velocities vary along high-symmetry directions [36–38]. The anisotropy of the Dirac cone might provide anisotropic carrier mobility, thus leading to the realization of direction-dependent transport for quantum devices [36,38]. A few materials harboring anisotropic surface Dirac cones have been reported [28,39–43]. However, examples of 2D anisotropic Dirac cones are limited in 3D materials.

In this paper, we investigate the electronic band structures of the (001) surface of Ti_2Te_2P using high-resolution vacuum ultraviolet ARPES and first-principles calculations. Our measurements reveal the presence of anisotropic surface Dirac cones at the $\bar{M}$ point and nodal-line-like features along

*Corresponding author: Madhab.Neupane@ucf.edu

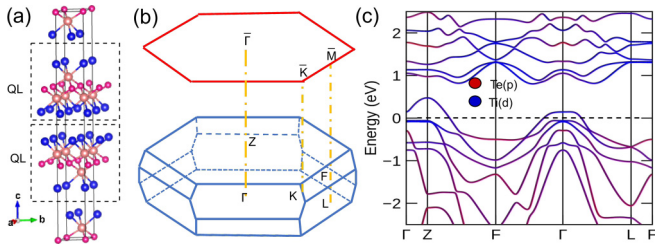

FIG. 1. Crystal structure and band-structure calculations of Ti_2Te_2P: (a) Crystal structure of Ti_2Te_2P stacked in hexagonal layers, in which blue, brown, and pink balls identify Te, Ti, and P atoms, respectively. The dotted rectangles enclose quintuple layers. (b) 3D bulk Brillouin zone (BZ) of single crystals and its projected hexagonal surface where the high-symmetry points are labeled. (c) First-principles calculation of the bulk bands with inclusion of spin-orbit coupling.

the $\bar{\Gamma}$-$\bar{M}$ direction. The experimental results are in excellent agreement with the first-principles calculations. Parity calculations reveal the band inversions at the Γ and the F point, indicating that the system is topologically rich. The anisotropic Dirac cones have the potential to be used in technological applications due to the different mobilities in a Dirac cone.

II. METHODS

Single crystals of Ti_2Te_2P were grown by the chemical vapor transport method as described in Refs. [44,45], and details of sample characterizations are described in the Supplemental Material (SM) note 1 [46].

Synchrotron-based ARPES measurements were performed at the Advanced Light Source (ALS) beamline 10.0.1 equipped with Scienta R4000, ALS beamline 4.0.3 equipped with R8000 hemispherical electron analyzers, and at the SIS-HRPES end-station at the Swiss Light Source (SLS) equipped with Scienta R4000. Similarly, helium-lamp-based ARPES measurements were performed at the Laboratory for Advanced Spectroscopic Characterization of Quantum Materials (LASCQM) with a R3000 hemispherical analyzer at the University of Central Florida. The angular and energy resolutions were set to be better than 0.2° and 20 meV, respectively. The electronic structure calculations and structural optimization were carried out within the density-functional formalism, which are described in SM note 2 [46–51].

III. RESULTS AND ANALYSIS

We begin our discussion by presenting the crystal structure of Ti_2Te_2P in Fig. 1(a). It is isostructural to Bi_2Te_2Se, and crystallizes in a rhombohedral crystal structure with lattice parameters $a = 3.6387(2)$ Å, $c = 28.486(2)$ Å, and space group $R\bar{3}m$ (No. 166), each unit cell consisting of three quintuple atomic layers separated by van der Waals gaps [44]. The phosphorus and tellurium atoms are arranged in hexagonal layers stacked along the hexagonal c axis in a sequence with two layers of tellurium followed by a single layer of phosphorus, and the gap is filled by titanium as shown in Fig. 1(a). The (001) plane is the natural cleaving plane in this compound due to the atomic layers along the c axis. A three-dimensional BZ and its projection to 2D along the [001] direction are presented in Fig. 1(b), which illustrates the hexagonal symmetry of the (001) surface BZ. Figure 1(c) shows the bulk band calculation of Ti_2Te_2P [with spin-orbit coupling (SOC)] along the high-symmetry directions which includes four time-reversal invariant momenta (TRIM) points. It shows a holelike band around the Γ point. A band is seen crossing the chemical potential at the Γ point indicating the semimetallic behavior, which is flat in the vicinity of the Fermi level at the Γ point. Our detailed electronic structure calculations show the occurrence of bulk band inversion both at the Γ and the F point. These band inversions are between Ti p and Te d states and involve different sets of bands (see SM [46]). A bulk band inversion at the F point takes place between Ti p and Te d bands around 750 meV below the Fermi level, which agrees well with both the calculated and observed Dirac surface state at the $\bar{M}$ point. This surface state is of the strong TI type, since our calculated Z_2 indices for this case are (1; 000) (see SM [46]). Unlike the other sister compounds of this family (Zr_2Te_2P, Hf_2Te_2P), Ti_2Te_2P does not possess band inversion above the chemical potential at the zone center. The parity analysis of this system shows that a strong TI state exists at the Γ point and at the M point (see SM for the parity calculation [46]). Our calculations indicate that the band inversion between different bulk bands at the Γ point also leads to strong TI topology with $\mathbb{Z}_2$ again (1; 000). Remarkably, this band inversion takes place near a similar binding energy as the one responsible for the Dirac surface state at the $\bar{M}$ point (see SM [46]).

Figure 2 illustrates the detailed electronic structures of experimentally measured Ti_2Te_2P by using synchrotron-based high-resolution ARPES. In Fig. 2(a), the Fermi-surface map is presented which has a sixfold flower petal shape as a consequence of the presence of threefold rotational and inversion symmetry. At the $\bar{\Gamma}$ point, a circular-shaped energy pocket can be seen due to the holelike band that crosses the chemical potential. Furthermore, a constructed BZ is presented in which the high-symmetry points are labeled. The photoemission spectra obtained from ARPES measurements suggest that petal-shaped Fermi pockets are surface originated as they do not disperse significantly with photon energies (see SM [46]). The impacts of the matrix element effects are noticeable, leading to nonuniform spectral intensities. Furthermore, petal-like features coming from the secondary BZ can be observed at the edges. The ARPES measured Fermi surface of Ti_2Te_2P is similar to the Fermi surface of Zr_2Te_2P and Hf_2Te_2P [28–30]. The energy contours delineate how the band dispersions evolve with the binding energies. The energy pockets at the $\bar{\Gamma}$ point grow bigger with binding energy, indicating the hole nature of the bands at the $\bar{\Gamma}$ point. This hexagonal BZ has six $\bar{M}$ points at the center of the elliptical Fermi pockets. The diameters of the elliptical petal diminish with binding energies. At the binding energy of 750 meV, the elliptical features collapse into lines. Furthermore, the linelike feature seen along the $\bar{\Gamma}$-$\bar{M}$ direction forms nodal-line-like states as it is the crossing point of bulk Dirac dispersions (see SM [46]). Interestingly, there are an even number of topological nontrivial surface states at the $\bar{\Gamma}$ point and one

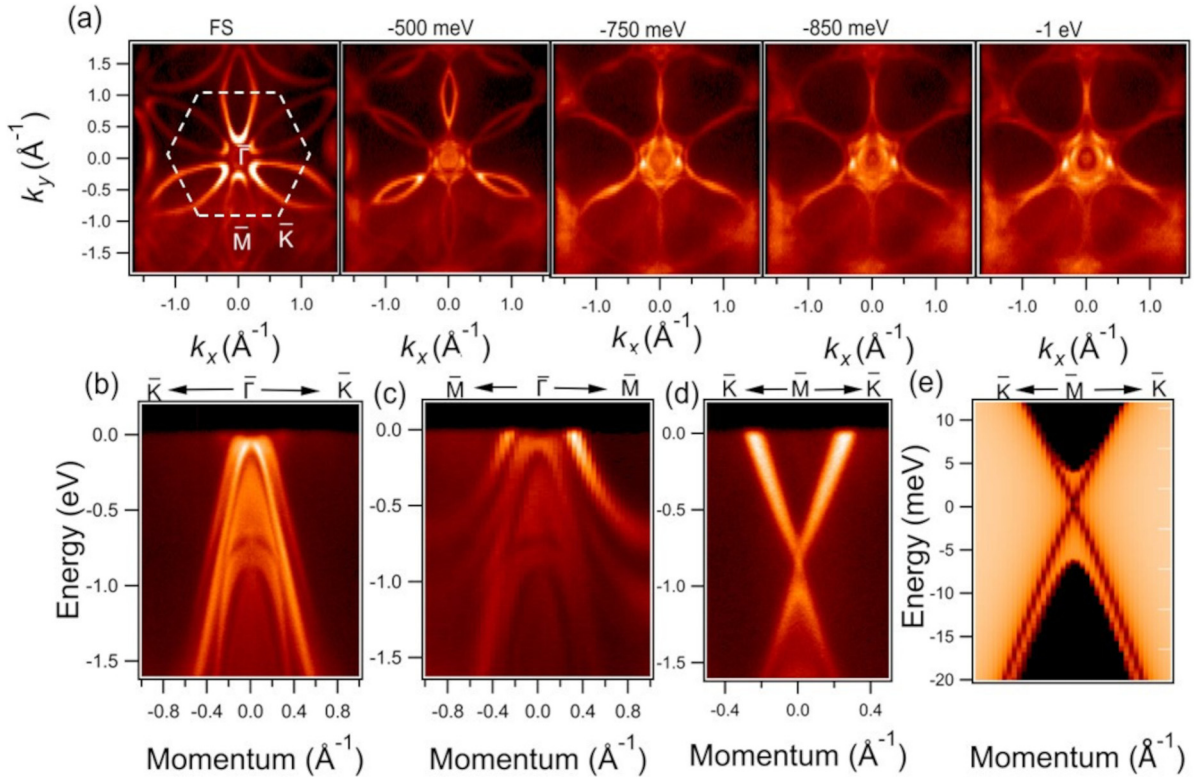

FIG. 2. Fermi-surface map and electronic band dispersions of Ti_2Te_2P: (a) Fermi-surface map and constant energy contours at different binding energies measured at a photon energy of 100 eV. The white-colored hexagonal shape is a constructed BZ in order to identify the high-symmetry points. Band dispersion along the (b) $\bar{K}$-$\bar{\Gamma}$-$\bar{K}$, (c) $\bar{M}$-$\bar{\Gamma}$-$\bar{M}$, and (d) $\bar{K}$-$\bar{M}$-$\bar{K}$ directions. (e) Calculated band dispersion map along the $\bar{K}$-$\bar{M}$-$\bar{K}$ direction. In the energy axis, the Dirac point is set as zero. All the measured data were collected at ALS beamline 4.0.3 at a temperature of 16 K.

at the $\bar{M}$ point, which provide the condition for Dirac-node arcs [30]. However, we do not observe gapped bulk Dirac cones in the vicinity of the $\bar{\Gamma}$ as seen in Hf_2Te_2P, probably due to weaker spin-orbit coupling, or due to energy resolution limitations obscuring the gap in the photoemission intensity plot. The node arc feature is protected by in-plane time-reversal invariance similar to its sister compound Hf_2Te_2P. In order to study the dispersion maps along the high-symmetry axes, we present ARPES measurements of energy dispersion along the high-symmetry directions. Figure 2(b) shows band structures along the $\bar{K}$-$\bar{\Gamma}$-$\bar{K}$ direction. Holelike bands are seen in the vicinity of the Fermi level. Another band exists almost 750 meV below the Fermi level, which can be seen in the bulk band calculations. Figure 2(c) displays the dispersion map along the $\bar{M}$-$\bar{\Gamma}$-$\bar{M}$, in which holelike bands can be seen. The slab calculations (see SM [46]) suggest that most of the bands are bulk originated, whereas a pair of surface-originated bands are buried within the bulk bands.

In Fig. 2(d), we present the dispersion map along the $\bar{K}$-$\bar{M}$-$\bar{K}$ direction in which we observe a Dirac state at the binding energy of 750 meV. Our photon energy-dependent measurements suggest a surface-originated Dirac cone, however, the slab calculations [see Fig. 2(e)] suggest the presence of bulk bands. The bulk bands and surface bands, however, cannot be resolved in the present resolution.

To show the anisotropic Dirac cones at the $\bar{M}$ points, we have taken dispersion maps along different directions at the $\bar{M}$ point which have different Fermi velocities. Figure 3(a) shows the Fermi-surface map in which one $\bar{M}$ point is chosen as a reference point to demonstrate the anisotropy of the Dirac state at the $\bar{M}$ point. The Dirac cones are formed by the elliptical-shaped petals at the Fermi surface. In Fig. 3(b), dispersion maps along the different directions are presented, which make angles of 0°–80° at an interval of 20°. The dispersion maps delineate the presence of anisotropic Dirac cones.

To quantitatively determine the anisotropy of the Dirac cone in Ti_2Te_2P, we have performed a detailed analysis along both cut 1, i.e., along the $\bar{K}$-$\bar{M}$-$\bar{K}$ high-symmetry direction, and cut 6 which is rotated 60° with respect to the $\bar{K}$-$\bar{M}$-$\bar{K}$ direction [see Figs. 4(a)–4(c)]. Figures 4(a) and 4(b) show the momentum distribution curves (MDCs) (red open circles) which are extracted from the ARPES dispersions. In order to fit the obtained MDCs, Gaussian-Lorentzian (GL) product functions have been used. The Gaussian part represents primarily the energy resolution of the instrument and the lifetime broadening of the photoelectrons, whereas the core holes are captured by the Lorentzian width [52,53]. The fitted MDCs as shown in Figs. 4(a) and 4(b) show accurate fits up to around 750 meV, i.e., near the Dirac point. From the obtained results one can see that along cut 1, the dispersion of the topological surface states (TSSs) follows a linear behavior whereas along cut 4 the dispersion of the TSSs deviated quite strongly from the linear behavior [see Fig. 4(d)]. The different behavior of the dispersion of the TSSs along the different directions thus clearly shows the anisotropic dispersion of the TSSs.

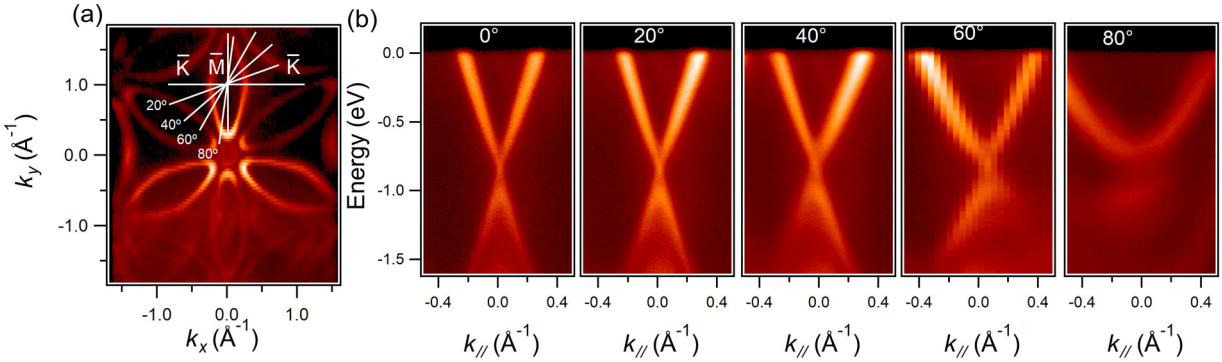

FIG. 3. Experimental observation of anisotropic Dirac cone: (a) Fermi-surface map in which white-colored lines are drawn via the $\bar{M}$ point to show angles of dispersion maps with respect to the $\bar{K}$-$\bar{M}$-$\bar{K}$ direction. (b) Dispersion maps along different orientations; angles with respect to the $\bar{K}$-$\bar{M}$-$\bar{K}$ direction are noted on the top of the plots. All data were collected at ALS beamline 4.0.3 at a photon energy of 100 eV.

The magnitude of the Fermi velocity associated with cut 1 is almost double that of cut 4. Figure 4(e) displays the change in the $k_{\parallel}$ vector as a function of the rotation angle where the rotation has been performed with respect to the high-symmetry direction $\bar{K}$-$\bar{M}$-$\bar{K}$; it clearly shows a significant increase of the $k_{\parallel}$ wave vector above 40° rotation.

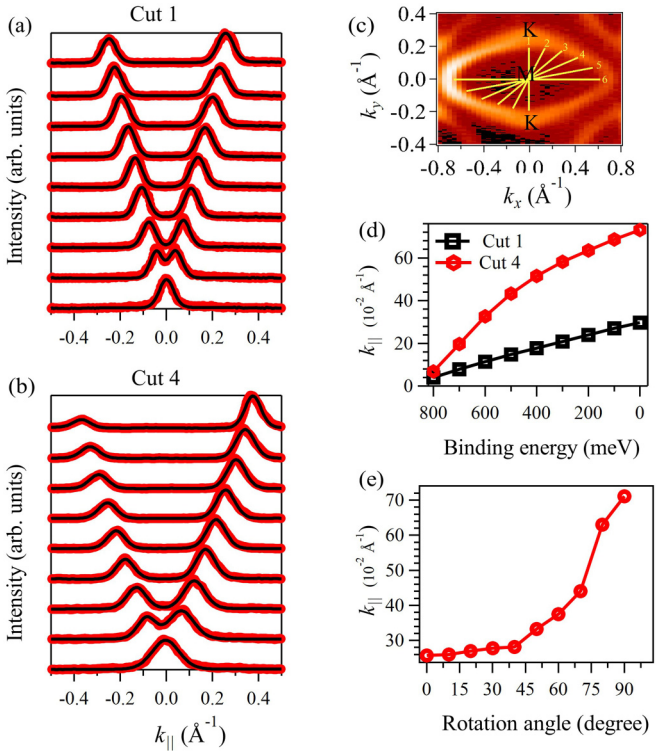

FIG. 4. Demonstration of anisotropy in a Dirac cone: (a) Experimental momentum distribution curves (MDCs) (red open circles) integrated within 4 meV of the corresponding binding energy and fitted (black solid lines) to the experimental MDCs along cut 1 as shown in (c). (b) Same as (a) but along cut 4, i.e., rotated by 60° with respect to the $\bar{K}$-$\bar{M}$-$\bar{K}$ direction. (c) Zoomed-in view of the Fermi surface where the yellow lines 1–6 indicate cut directions in the interval of 20°. (d) The $k_{\parallel}$ dispersions as a function of binding energy. The coordinates are obtained from the MDC plots from (a) and (b). (e) The $k_{\parallel}$ values as a function of rotation angles with respect to the $\bar{K}$-$\bar{M}$-$\bar{K}$ direction.

IV. DISCUSSION

The anisotropic surface Dirac cone in a 3D system has been overlooked despite substantial work done on the tilted bulk Dirac cones in semimetallic systems. The anisotropic Dirac cone at the $\bar{M}$ point of Ti_2Te_2P is a consequence of the petal-shaped energy pocket at the $\bar{M}$ point in the BZ, due to which the Fermi velocities vary along the directions of the dispersion maps. Furthermore, the warping of the Dirac cone can be seen along the direction of the $\bar{\Gamma}$ potentially due to bulk bands which exist along the $\bar{\Gamma}$-$\bar{M}$ direction. The anisotropy of TSSs in some materials has been observed [7,41,43,54–56], which is attributed to the spin-dependent scattering giving rise to anisotropic scattering rates of the surface-state electrons, however, the role of spin-dependent scattering in Ti_2Te_2P is yet to be revealed. Importantly, materials with anisotropic surface Dirac cones could be a platform that provide a direction-dependent transport. It requires further explorations in such materials.

V. CONCLUSION

In conclusion, we observe anisotropic Dirac cones at the $\bar{M}$ points in Ti_2Te_2P material. Our $\mathbb{Z}_2$ calculations identify this system as topologically nontrivial. The presence of nodal-line-like features along the $\bar{\Gamma}$-$\bar{M}$ direction in addition to the anisotropic Dirac cones makes this system topologically rich. Our study provides an archetype system for the understanding of the 221-tetradymite system and we anticipate that it will stimulate further research interests in this class of material.

ACKNOWLEDGMENTS

M.N. acknowledges support from the Air Force Office of Scientific Research under Award No. FA9550-17-1-0415, the Air Force Office of Scientific Research MURI (Grant No. FA9550-20-1-0322), and the National Science Foundation (NSF) CAREER Award No. DMR-1847962. A.K.N., A.A., and P.M.O. acknowledge support from the Swedish Research Council (VR) and from the Knut and Alice Wallenberg Foundation (Grant No. 2015.0060). Computational resources were provided by the Swedish National Infrastructure for computing (SNIC) (Grant No. 2018-05973). A.K.N. acknowledges the support of Department of Atomic Energy (DAE) and

Science and Engineering Research Board (SERB) research grant (Grant No. SRG/2019/000867) of the Government of India. We thank Sung-Kwan Mo and Jonathan Denlinger for beamline assistance at the LBNL. This research used resources of the Advanced Light Source, a U.S. DOE Office of Science User Facility under Contract No. DE-AC02-05CH11231. We thank Nicholas Clark Plumb for beamline assistance at the SLS, PSI.

[1] M. Z. Hasan and C. L. Kane, Rev. Mod. Phys. **82**, 3045 (2010).
[2] X.-L. Qi and S.-C. Zhang, Rev. Mod. Phys. **83**, 1057 (2011).
[3] M. Z. Hasan, S.-Y. Xu, and M. Neupane, Topological insulators, topological Dirac semimetals, topological crystalline insulators, and topological Kondo insulators, in *Topological Insulators: Fundamentals and Perspectives*, edited by F. Ortmann, S. Roche, and S. O. Valenzuela (Wiley, Hoboken, NJ, 2015).
[4] A. Bansil, H. Lin, and T. Das, Rev. Mod. Phys. **88**, 021004 (2016).
[5] L. Fu, C. L. Kane, and E. J. Mele, Phys. Rev. Lett. **98**, 106803 (2007).
[6] Y. Xia, D. Qian, D. Hsieh, L. Wray, A. Pal, H. Lin, A. Bansil, D. Grauer, Y. S. Hor, R. J. Cava, and M. Z. Hasan, Nat. Phys. **5**, 398 (2009).
[7] Y. L. Chen, J. G. Analytis, J.-H. Chu, Z. K. Liu, S.-K. Mo, X. L. Qi, H. J. Zhang, D. H. Lu, X. Dai, Z. Fang, S. C. Zhang, I. R. Fisher, Z. Hussain, and Z.-X. Shen, Science **325**, 178 (2009).
[8] Y. Ando and L. Fu, Annu. Rev. Condens. Matter Phys. **6**, 361 (2015).
[9] Z. Wang, H. Weng, Q. Wu, X. Dai, and Z. Fang, Phys. Rev. B **88**, 125427 (2013).
[10] M. Neupane, S.-Y. Xu, R. Sankar, N. Alidoust, G. Bian, C. Liu, I. Belopolski, T.-R. Chang, H.-T. Jeng, H. Lin, A. Bansil, F. Chou, and M. Z. Hasan, Nat. Commun. **5**, 3786 (2014).
[11] B.-J. Yang and N. Nagaosa, Nat. Commun. **5**, 4898 (2014).
[12] S. M. Young, S. Zaheer, J. C. Y. Teo, C. L. Kane, E. J. Mele, and A. M. Rappe, Phys. Rev. Lett. **108**, 140405 (2012).
[13] S.-Y. Xu, I. Belopolski, N. Alidoust, M. Neupane, G. Bian, C. Zhang, R. Sankar, G. Chang, Z. Yuan, C.-C. Lee *et al.*, Science **349**, 613 (2015).
[14] H. Weng, C. Fang, Z. Fang, B. A. Bernevig, and X. Dai, Phys. Rev. X **5**, 011029 (2015).
[15] M. Neupane, I. Belopolski, M. M. Hosen, D. S. Sanchez, R. Sankar, M. Szlawska, S.-Y. Xu, K. Dimitri, N. Dhakal, P. Maldonado *et al.*, Phys. Rev. B **93**, 201104(R) (2016).
[16] M. M. Hosen, K. Dimitri, I. Belopolski, P. Maldonado, R. Sankar, N. Dhakal, G. Dhakal, T. Cole, P. M. Oppeneer, D. Kaczorowski *et al.*, Phys. Rev. B **95**, 161101 (2017).
[17] L. Fu, Phys. Rev. Lett. **106**, 106802 (2011).
[18] M. Neupane, N. Alidoust, S. Y. Xu, T. Kondo, Y. Ishida, D. J. Kim, C. Liu, I. Belopolski, Y. J. Jo, T. R. Chang *et al.*, Nat. Commun. **4**, 2991 (2013).
[19] M. Neupane, S. Basak, N. Alidoust, S. Y. Xu, C. Liu, I. Belopolski, G. Bian, J. Xiong, H. Ji, S. Jia *et al.*, Phys. Rev. B **88**, 165129 (2013).
[20] S.-Y. Xu, M. Neupane, C. Liu, D. Zhang, A. Richardella, L. A. Wray, N. Alidoust, M. Leandersson, T. Balasubramanian, J. Sánchez-Barriga *et al.*, Nat. Phys. **8**, 616 (2012).
[21] Z. Ren, A. A. Taskin, S. Sasaki, K. Segawa, and Y. Ando, Phys. Rev. B **82**, 241306(R) (2010).
[22] H. Ji, J. M. Allred, M. K. Fuccillo, M. E. Charles, M. Neupane, L. A. Wray, M. Z. Hasan, and R. J. Cava, Phys. Rev. B **85**, 201103(R) (2012).
[23] C. Pauly, G. Bihlmayer, M. Liebmann, M. Grob, A. Georgi, D. Subramaniam, M. R. Scholz, J. Sánchez-Barriga, A. Varykhalov, S. Blügel, O. Rader, and M. Morgenstern, Phys. Rev. B **86**, 235106 (2012).
[24] C.-K. Lee, C.-M. Cheng, S.-C. Weng, W.-C. Chen, K.-D. Tsuei, S.-H. Yu, M. M.-C. Chou, C.-W. Chang, L.-W. Tu, H.-D. Yang, C.-W. Luo, and M. M. Gospodinov, Sci. Rep. **6**, 36538 (2016).
[25] J. E. Moore, Nature (London) **464**, 194 (2010).
[26] M. Neupane, A. Richardella, J. Sánchez-Barriga, S. Xu, N. Alidoust, I. Belopolski, C. Liu, G. Bian, D. Zhang, D. Marchenko *et al.*, Nat. Commun. **5**, 3841 (2014).
[27] H. J. Zhang, C. X. Liu, X. L. Qi, X. Dai, Z. Fang, and S. C. Zhang, Nat. Phys. **5**, 438 (2009).
[28] H. Ji, I. Pletikosić, Q. D. Gibson, G. Sahasrabudhe, T. Valla, and R. J. Cava, Phys. Rev. B **93**, 045315 (2016).
[29] K. W. Chen, N. Aryal, J. Dai, D. Graf, S. Zhang, S. Das, P. Le Fèvre, F. Bertran, R. Yukawa, K. Horiba, H. Kumigashira, E. Frantzeskakis, F. Fortuna, L. Balicas, A. F. Santander-Syro, E. Manousakis, and R. E. Baumbach, Phys. Rev. B **97**, 165112 (2018).
[30] M. M. Hosen, K. Dimitri, A. K. Nandy, A. Aperis, R. Sankar, G. Dhakal, P. Maldonado, F. Kabir, C. Sims, F. Chou *et al.*, Nat. Commun. **9**, 3002 (2018).
[31] J. Dai, E. Frantzeskakis, N. Aryal, K.-W. Chen, F. Fortuna, J. E. Rault, P. Le Fèvre, L. Balicas, K. Miyamoto, T. Okuda, E. Manousakis, R. E. Baumbach, and A. F. Santander-Syro, Phys. Rev. Lett. **126**, 196407 (2021).
[32] A. A. Soluyanov, D. Gresch, Z. Wang, Q. Wu, M. Troyer, X. Dai, and B. A. Bernevig, Nature (London) **527**, 495 (2015).
[33] H. Huang, S. Zhou, and W. Duan, Phys. Rev. B **94**, 121117(R) (2016).
[34] C. Le, S. Qin, X. Wu, X. Dai, P. Fu, C. Fang, and J. Hu, Phys. Rev. B **96**, 115121 (2017).
[35] T.-R. Chang, S.-Y. Xu, D. S. Sanchez, W.-F. Tsai, S.-M. Huang, G. Chang, C.-H. Hsu, G. Bian, I. Belopolski, Z.-M. Yu *et al.*, Phys. Rev. Lett. **119**, 026404 (2017).
[36] B. Feng, J. Zhang, S. Ito, M. Arita, C. Cheng, L. Chen, K. Wu, F. Komori, O. Sugino, K. Miyamoto *et al.*, Adv. Mater. **30**, 1704025 (2018).
[37] H.-Y. Lu, A. S. Cuamba, S.-Y. Lin, L. Hao, R. Wang, H. Li, Y. Y. Zhao, and C. S. Ting, Phys. Rev. B **94**, 195423 (2016).
[38] Y. Zhao, X. Li, J. Liu, C. Zhang, and Q. Wang, J. Phys. Chem. Lett. **9**, 1815 (2018).
[39] J. Park, G. Lee, F. Wolff-Fabris, Y. Y. Koh, M. J. Eom, Y. K. Kim, M. A. Farhan, Y. J. Jo, C. Kim, J. H. Shim, and J. S. Kim, Phys. Rev. Lett. **107**, 126402 (2011).
[40] B. Feng, J. Zhang, S. Ito, M. Arita, C. Cheng, L. Chen, K. Wu, F. Komori, O. Sugino, K. Miyamoto *et al.*, Sci. Rep. **4**, 5385 (2014).
[41] Q. D. Gibson, D. Evtushinsky, A. N. Yaresko, V. B. Zabolotnyy, M. N. Ali, M. K. Fuccillo, J. Van den Brink, B. Büchner, R. J. Cava, and S. V. Borisenko, Sci. Rep. **4**, 5168 (2014).

[42] F. Virot, R. Hayn, M. Richter, and J. van den Brink, Phys. Rev. Lett. **106**, 236806 (2011).
[43] W. Zhang, R. Yu, W. Feng, Y. Yao, H. Weng, X. Dai, and Z. Fang, Phys. Rev. Lett. **106**, 156808 (2011).
[44] F. Philipp, P. Schmidt, M. Ruck, W. Schnelle, and A. Isaeva, J. Solid State Chem. **181**, 2859 (2008).
[45] J. S. Oh, H.-S. Yu, C.-J. Kang, S. Sinn, M. Han, Y. J. Chang, B.-G. Park, K. Lee, B. I. Min, S. W. Kim, H.-D. Kim, and T. W. Noh, Chem. Mater. **28**, 7570 (2016).
[46] See Supplemental Materials at http://link.aps.org/supplemental/10.1103/PhysRevB.106.125124 for photon energy-dependent measurements, different direction dispersion maps, constant energy contours, etc.
[47] G. Kresse and J. Furthmüller, Phys. Rev. B **54**, 11169 (1996).
[48] G. Kresse and J. Furthmüller, Comput. Mater. Sci. **6**, 15 (1996).
[49] J. P. Perdew, K. Burke, and M. Ernzerhof, Phys. Rev. Lett. **77**, 3865 (1996).
[50] G. Kresse, and D. Joubert, Phys. Rev. B **59**, 1758 (1999).
[51] P. E. Blöchl, Phys. Rev. B **50**, 17953 (1994).
[52] T. Valla, A. V. Fedorov, P. D. Johnson, B. O. Wells, S. L. Hulbert, Q. Li, G. D. Gu, and N. Koshizuka, Science **285**, 2110 (1999).
[53] T. Valla, Z.-H. Pan, D. Gardner, and Y. S. Lee, and S. Chu, Phys. Rev. Lett. **108**, 117601 (2012).
[54] K. Kuroda, M. Arita, K. Miyamoto, M. Ye, J. Jiang, A. Kimura, E. E. Krasovskii, E. V. Chulkov, H. Iwasawa, T. Okuda *et al.*, Phys. Rev. Lett. **105**, 076802 (2010).
[55] S. Souma, K. Kosaka, T. Sato, M. Komatsu, A. Takayama, T. Takahashi, M. Kriener, K. Segawa, and Y. Ando, Phys. Rev. Lett. **106**, 216803 (2011).
[56] J. Sánchez-Barriga, M. R. Scholz, E. Golias, E. Rienks, D. Marchenko, A. Varykhalov, L. V. Yashina, and O. Rader, Phys. Rev. B **90**, 195413 (2014).